

## Research Article

# Simultaneous Shape and Stacking Sequence Optimization of Laminated Composite Free-Form Shells Using Multi-Island Genetic Algorithm

Bingbing San , Zhi Xiao, and Ye Qiu

*College of Civil and Transportation Engineering, Hohai University, Nanjing 210098, China*

Correspondence should be addressed to Bingbing San; [sanbingbing@163.com](mailto:sanbingbing@163.com)

Received 8 June 2019; Accepted 28 August 2019; Published 22 October 2019

Academic Editor: Fabrizio Paolacci

Copyright © 2019 Bingbing San et al. This is an open access article distributed under the Creative Commons Attribution License, which permits unrestricted use, distribution, and reproduction in any medium, provided the original work is properly cited.

A simultaneous shape and stacking sequence optimization algorithm is presented for laminated composite free-form shells, by which the coupled effect of shape and stacking sequence can be considered. The optimization objective is determined as maximizing fundamental natural frequency to obtain largest stiffness of shells. Nonuniform rational B-spline (NURBS) is employed to represent free-form geometrical shapes. The coordinates of NURBS control points and fiber orientations are set up as continuous and discrete optimization variables, respectively, and optimized simultaneously. To improve the efficiency of the mixed continuous-discrete optimization, multi-island genetic algorithm (MIGA) is employed to search for the global result. Through several numerical examples, the performance of the proposed approach is demonstrated in comparison with the two-phase optimization method; the effect of boundary conditions and the setup of control points on optimal results are investigated, respectively.

## 1. Introduction

Fiber-reinforced laminated composites have gained large interest for use in civil structures and aerospace engineering due to their high modulus/weight, strength/weight ratios, and excellent designability [1, 2]. In recent years, laminated composite structures are increasingly used in shape-resistant forms to improve their efficiency [3]. The free-form shells are such a typical example. The term “free-form” is concerned with the geometrical shapes that cannot be represented by certain mathematical formulas or their combination [4, 5], which is used to distinguish them from those traditional shells, e.g., cylindrical and conical shells. One of the important features of free-form shells is that their mechanical properties, as well as manufacturing or operational costs, strongly depending on their geometrical shapes. In particular for laminated composite free-form shells, their performance is affected by the shape together with the stacking sequence. Therefore, the desired efficiency of laminated

composite free-form shells can be obtained by two ways: shape optimization and stacking sequences optimization.

Shape optimization is an approach to find the optimal geometry of a structure in order to capture a desired performance, subject to some given constraints. In the last few decades, numerical optimization methods to solve for optimal shapes of free-form shells have been developed. In a typical numerical shape optimization method, parameterized geometry presentation is first implemented to provide adequate geometrical description with the least amount of parameters [6]. Then, numerical methods such as finite element method (FEM) are usually employed to obtain the structural response of the forward system and compute the objective and constraint values. After that, the optimization algorithm is adopted to search for the optima. Following these procedure, some efforts were made in shape optimization of free-form shells.

Bletzinger et al. [7] optimized free-form shells for structural stiffness under given loadings using numerical

methods, which is emerged with physical experiments. In their following work, they presented an isogeometric shape optimization method for shell structures applying sensitivity weighting and semianalytical analysis [8]. Ohmori and Hamada [9] combined nonuniform rational B-spline (NURBS) with the genetic algorithm (GA) as well as the gradient method to perform shape optimization of free-form shells, in which the objectives are set up as minimum strain energy and minimum geometrical deviation from the prescribed shape. Shimoda and Liu [10] employed a non-parametric method to obtain desired vibration displacement of free-form shells. In [11], this optimization objective is extended to maximizing vibration eigenvalue and minimizing dynamic responses. Winslow et al. [12] presented a design tool for synthesis of optimal free-form structures using a multiobjective GA to vary rod directions over the surface in response to two or more load cases.

Meanwhile, many studies were carried out on the stacking sequence optimization of laminated shells. Most of them focused on traditional types of composite shells, such as cylindrical, conical, and spherical composite shells. Kriegesmann et al. [13] optimized ply angles of laminated composite cylindrical shells with an objective to maximize buckling load. Abouhamze and Shakeri [14] carried out multiobjective optimization for optimal stacking sequence of laminated cylindrical panels, with respect to the fundamental natural frequency and critical buckling load. Ameri et al. [15] investigated the stacking sequence of laminated cylindrical shells to maximize their fundamental natural frequency. Zhi et al. [16] combined GA and simulated annealing (SA) to optimize the configuration of advanced composite grid-stiffened conical shells to minimize the weight under constraint with respect to critical buckling load. Mingfa et al. [17] used an adoptive SA to minimize the weight of a cone-shaped composite tank with ply orientation angles and the number of layers as optimization variables. Topal [18] optimized fiber orientations to maximize the fundamental frequency of laminated composite spherical shells. Nascimbene [19] optimized a free-form sail composite shell in orientation angles and thickness of fibers for multiple objectives. One can refer to [20, 21] for more works on this topic.

It can be seen that either shape optimization or stacking sequence optimization has been studied widely. However, it is noted that there exists limited research considering both shape and stacking sequence optimization. Wu and Burgueno [3] proposed an integral approach to shape and laminate stacking sequence optimization of composite free-form shells, which is implemented in a two-level procedure: Level 1—shape optimization and laminate-property optimization using gradient-based method, followed by Level 2—laminate stacking sequence optimization using GA. In this approach, the discrete variables with respect to stacking sequence were alternatively described by continuous variables of the lamination material parameters; in which case, the laminate parameters are not independent and cannot be arbitrarily prescribed [21].

Honda et al. [22] optimized the shape and stacking sequence of laminated composite shells simultaneously. However, in their study, the geometrical shape of shells is

defined by a cubic polynomial, which only creates a limited set of surfaces and cannot guarantee their smoothness except when the shell is shallow.

Motivated by the works above, this paper proposes a simultaneous shape and stacking sequence optimization method for laminated free-form shells with objective to maximize the fundamental frequency. In this method, NURBS is employed to represent the geometrical shape of shells. The coordinates of control points and fiber orientations are set up as continuous and discrete optimization variables, respectively, and optimized simultaneously. Due to the complex design space involving both continuous and discrete design variables, the multi-island genetic algorithm (MIGA) is employed to search for the global result and improve computational efficiency. Several numerical examples are carried out to demonstrate the proposed method and provide insight into the simultaneous optimization results for different boundary conditions and various locations of control points.

The paper is organized as follows: Section 2 presents an introduction to NURBS. In Section 3, FEM is described to solve fundamental natural frequency. Section 4 states the optimization problem and presents MIGA, and in Section 5, results of several numerical examples are reported and discussed. Some conclusions of this work are provided in Section 6.

## 2. Geometrical Representation of Free-Form Shapes

Different from regular shells, the geometric shape of free-form shells can rarely be represented by an explicit function. Thus, shape parameterization is needed to describe their arbitrary shapes with desired smoothness obtained by control points, in which case the control points are used as design variables. Here, NURBS functions are employed to represent the shape of shells, which are developed from B-spline and have been widely applied in computer-aided design (CAD) [23], finite element discretization [24], and others. NURBS can present complex free-form shapes. And from our optimization perspective, the use of NURBS allows for a simple integration of smooth shape representation into existing finite element codes. This section gives a brief introduction to NURBS surface. For more details, one can refer to [24, 25]. The NURBS surface is defined by B-spline basis functions, coordinates of control points, and their respective weights, as follows:

$$S(u, v) = \frac{\sum_{i=1}^m \sum_{j=1}^n P_{i,j} \omega_{i,j} N_{i,k}(u) N_{j,g}(v)}{\sum_{i=1}^m \sum_{j=1}^n \omega_{i,j} N_{i,k}(u) N_{j,g}(v)}, \quad (1)$$

where  $P_{ij}$  are the coordinates of the control points, which form a  $m \times n$  point grid,  $\omega_{ij}$  is their respective weights, and  $N_{i,k}(u)$  and  $N_{j,g}(v)$  represent the B-spline basis functions of degrees  $k$  and  $g$  in the two directions, respectively.

$N_{j,g}(u)$  and  $N_{j,g}(v)$  are defined in the same way. Considering the size of paper, only  $N_{j,g}(u)$  is given. It is defined in a parametric space of the so-called knot vector, where  $u_1 \leq u_2 \leq \dots \leq u_{m+k+1}$  are real numbers in the parametric space  $[0, 1]$ . To satisfy the Kronecker delta property at boundary points, a knot vector with  $k + 1$  knots at each ends

is adopted. Knots at the beginning and the end are repeated to make the basis interpolatory.  $N_{i,k}(u)$  is defined as the following recursive function:

$$N_{i,0}(u) = \begin{cases} 1, & u_i \leq u < u_{i+1}, \\ 0, & \text{otherwise,} \end{cases}$$

$$N_{i,k}(u) = \frac{u - u_i}{u_{i+k} - u_i} N_{i,k-1}(u) + \frac{u_{i+k+1} - u}{u_{i+k+1} - u_{i+1}} N_{i+1,k-1}(u), \quad k = 1, 2, 3, \dots \quad (2)$$

Figure 1 gives an example of control point grid and corresponding NURBS surface with assumption that weights of all control points are 1.0. From equations (1) and (2), it can be seen that the geometry of a NURBS surface is determined by the locations of control points and their respective weights. Any modification in them will change the geometric shape of the surface. However, the work presented in [26] showed that locations of the control points play a dominant role in changing shapes rather than their weights. Thus, in order to decrease the computational cost, authors only set up coordinates of control points as shape optimization variables while fixing their weights in optimization.

### 3. FEM Formulation of Laminate Shells

In this paper, laminate shells are formulated using FEM based on Mindlin–Reissner theory [27, 28]. The laminate model is shown in Figure 2 with the description of coordinate systems. Axes  $XYZ$  and axes  $xyz$  represent the global and local coordinate systems, respectively. Axes 123 represent the material principal coordinate system in the  $j$ th single layer, where axes 1 and 2 denote the longitudinal and transverse directions, respectively;  $\theta_j$  denotes the fiber angle, which represents the angle counterclockwise rotating from axis  $x$  to axis 1.

The element stiffness matrix  $\mathbf{K}^e$  of shells is defined in the local coordinate system ( $xyz$ ) as [28]

$$\mathbf{K}^e = \mathbf{K}_{mb}^e + \mathbf{K}_s^e = \int_{V^e} \mathbf{B}_p^T \mathbf{C}_p \mathbf{B}_p dV + \int_{V^e} \mathbf{B}_s^T \mathbf{C}_s \mathbf{B}_s dV, \quad (3)$$

where  $\mathbf{K}_{mb}^e$  denotes the combination of extensional, bending, and bending-extensional coupling stiffness matrices;  $\mathbf{K}_s^e$  denotes the shearing stiffness matrix;  $\mathbf{B}_p$  and  $\mathbf{B}_s$  are corresponding strain matrices;  $\mathbf{C}_p$  and  $\mathbf{C}_s$  are corresponding constitutive relation matrices; and  $V^e$  is the volume of elements.

The rest of this section focuses on the formulations of  $\mathbf{C}_p$  and  $\mathbf{C}_s$ , which present the features of laminate materials. Other formulations can be found in [28, 29].

For fiber-composite laminate materials, each lamina can be considered as an orthotropic layer. The constitutive relation in the material principal direction (see axes 1 and 2 in Figure 2) can be written as

$$\boldsymbol{\sigma}_m = \mathbf{Q} \boldsymbol{\varepsilon}_m, \quad (4)$$

where  $\boldsymbol{\sigma}_m$  and  $\boldsymbol{\varepsilon}_m$  denote the stress and strain vectors, respectively, and  $\mathbf{Q}$  denotes constitutive matrix, and they are written as

$$\boldsymbol{\sigma}_m = \begin{Bmatrix} \sigma_1 \\ \sigma_2 \\ \tau_{12} \\ \tau_{23} \\ \tau_{13} \end{Bmatrix}, \quad \boldsymbol{\varepsilon}_m = \begin{Bmatrix} \varepsilon_1 \\ \varepsilon_2 \\ \gamma_{12} \\ \gamma_{23} \\ \gamma_{13} \end{Bmatrix}, \quad \mathbf{Q} = \begin{bmatrix} \mathbf{Q}_{11} & \mathbf{Q}_{12} & 0 & 0 & 0 \\ & \mathbf{Q}_{22} & 0 & 0 & 0 \\ & & \mathbf{Q}_{66} & 0 & 0 \\ & & & \mathbf{Q}_{44} & 0 \\ \text{sym} & & & & \mathbf{Q}_{55} \end{bmatrix}. \quad (5)$$

The members of  $\mathbf{Q}$  are defined as

$$\left\{ \begin{array}{l} \mathbf{Q}_{11} = \frac{E_1}{1 - \nu_{12}\nu_{21}}, \\ \mathbf{Q}_{12} = \frac{\nu_{12}E_2}{1 - \nu_{12}\nu_{21}} = \frac{\nu_{21}E_1}{1 - \nu_{12}\nu_{21}}, \\ \mathbf{Q}_{22} = \frac{E_2}{1 - \nu_{12}\nu_{21}}, \\ \mathbf{Q}_{66} = G_{12}, \\ \mathbf{Q}_{44} = G_{23}, \\ \mathbf{Q}_{55} = G_{13}, \end{array} \right. \quad (6)$$

where  $E_1$  and  $E_2$  are the longitudinal and transverse elasticity moduli, respectively;  $\nu_{12}$  and  $\nu_{21}$  are the major and minor Poisson's ratios, respectively;  $G_{12}$  is in-plane shear modulus, while  $G_{23}$  and  $G_{13}$  are out-plane shear moduli.

As aforementioned, the fiber ply angle is the angle between material coordinate axis 1 and element local coordinate axis  $x$ . In this situation, the relation described in equation (4) needs to be transformed from the material coordinate system 123 to the element local coordinate system  $xyz$  as

$$\bar{\boldsymbol{\sigma}} = \bar{\mathbf{Q}} \bar{\boldsymbol{\varepsilon}}, \quad (7)$$

where  $\bar{\boldsymbol{\sigma}}$  and  $\bar{\boldsymbol{\varepsilon}}$  are stress and strain vectors in the local coordinate system, respectively, and  $\bar{\mathbf{Q}} = \mathbf{T}^T \mathbf{Q} \mathbf{T}$  is the transformed constitutive matrix, in which  $\mathbf{T}$  is the transformation matrix considering the fiber angle  $\theta_j$  of the  $j$ th lamina, written as

$$\mathbf{T} = \begin{bmatrix} \cos^2 \theta_j & \sin^2 \theta_j & \cos \theta_j \sin \theta_j & 0 & 0 \\ \sin^2 \theta_j & \cos^2 \theta_j & -\cos \theta_j \sin \theta_j & 0 & 0 \\ -\cos \theta_j \sin \theta_j & 2 \cos \theta_j \sin \theta_j & \cos^2 \theta_j - \sin^2 \theta_j & 0 & 0 \\ 0 & 0 & 0 & \cos \theta_j & \sin \theta_j \\ 0 & 0 & 0 & \sin \theta_j & \cos \theta_j \end{bmatrix}. \quad (8)$$

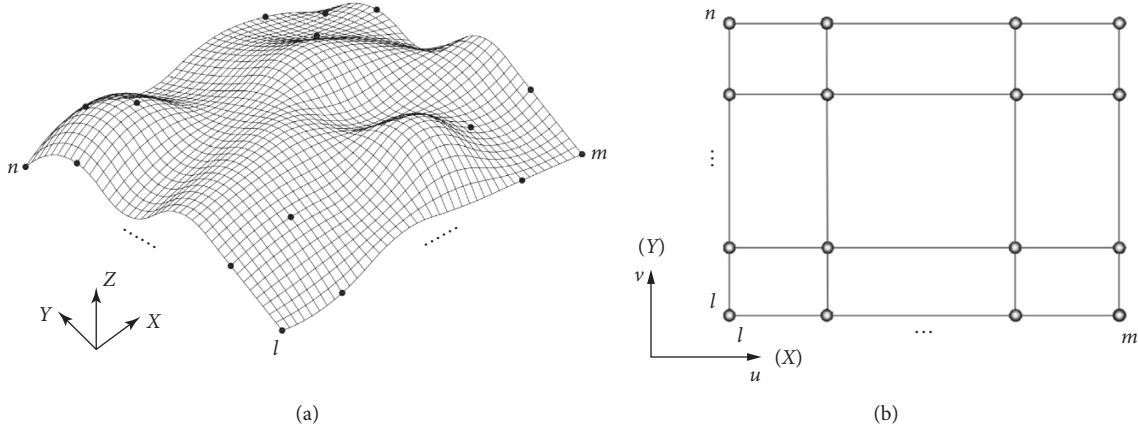


FIGURE 1: Example of NURBS surface. (a) NURBS surface. (b) Corresponding grid of control points.

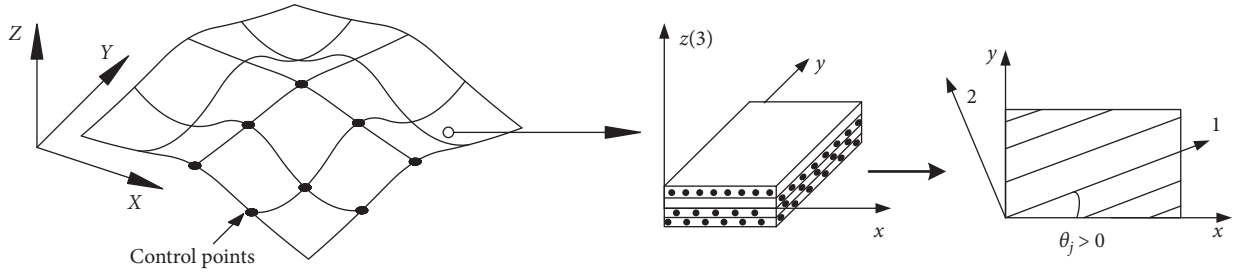


FIGURE 2: Illustration of the laminate model and coordinate systems.

A shell element can be seen as a combination of layers. In the local coordinate system, the authors assume that  $\mathbf{N} = [N_x \ N_y \ N_{xy}]^T$ ,  $\mathbf{M} = [M_x \ M_y \ M_{xy}]^T$ , and  $\mathbf{V} = [V_x \ V_y]^T$  are membrane force, bending moment, and transverse shear force vectors of the shell, respectively;  $\varepsilon_x^0$ ,  $\varepsilon_y^0$ , and  $\gamma_{xy}^0$  are the membrane strains;  $\kappa_x$ ,  $\kappa_y$ , and  $\kappa_{xy}$  are the bending strains; and  $\gamma_{yz}$  and  $\gamma_{xz}$  are the interlaminar shear strains. Relation between them is described by  $\mathbf{C}_p$  and  $\mathbf{C}_s$  as follows:

$$\begin{Bmatrix} N_x \\ N_y \\ N_{xy} \\ M_x \\ M_y \\ M_{xy} \end{Bmatrix} = \mathbf{C}_p \begin{Bmatrix} \varepsilon_x^0 \\ \varepsilon_y^0 \\ \gamma_{xy}^0 \\ \kappa_x \\ \kappa_y \\ \kappa_{xy} \end{Bmatrix} \quad (9)$$

$$= \begin{bmatrix} A_{11} & A_{12} & A_{16} & B_{11} & B_{12} & B_{16} \\ & A_{22} & A_{26} & B_{12} & B_{22} & B_{26} \\ & & A_{66} & B_{16} & B_{26} & B_{66} \\ & & & D_{11} & D_{12} & D_{16} \\ & & & & D_{22} & D_{26} \\ \text{sym} & & & & & D_{66} \end{bmatrix} \begin{Bmatrix} \varepsilon_x^0 \\ \varepsilon_y^0 \\ \gamma_{xy}^0 \\ \kappa_x \\ \kappa_y \\ \kappa_{xy} \end{Bmatrix}$$

$$\begin{Bmatrix} V_x \\ V_y \end{Bmatrix} = \mathbf{C}_s \begin{Bmatrix} \gamma_{yz} \\ \gamma_{xz} \end{Bmatrix} = \kappa \begin{bmatrix} A_{44} & A_{45} \\ A_{45} & A_{55} \end{bmatrix} \begin{Bmatrix} \gamma_{yz} \\ \gamma_{xz} \end{Bmatrix},$$

where  $\kappa$  is the shear correction factor matrix and  $A_{ij}$ ,  $B_{ij}$ , and  $D_{ij}$  are extensional and shear, bending-extensional, and bending stiffness coefficients, respectively, and defined as

$$(A_{ij}, B_{ij}, D_{ij}) = \int_{-h/2}^{h/2} (1, z, z^2) \bar{Q}_{ij} dz, \quad i, j = 1, 2, 6, \quad (10)$$

$$A_{ij} = \int_{-h/2}^{h/2} \bar{Q}_{ij} dz, \quad i, j = 4, 5,$$

where  $h$  is the thickness of the laminated shell.

Substituting equations (9) and (10) into equation (3), the element stiffness matrix  $\mathbf{K}^e$  of laminate shells can be obtained.

By using Hamilton's principle, the equation of motion for an undamped element without external force is obtained in the local coordinate system as

$$\mathbf{M}^e \ddot{\boldsymbol{\delta}}^e + \mathbf{K}^e \boldsymbol{\delta}^e = 0, \quad (11)$$

where  $\mathbf{M}^e$  denotes the local mass matrix and  $\boldsymbol{\delta}^e$  denotes the element displacement vector.

Through transformation from the local to global coordinate system, assembling the element mass and stiffness matrices in a general matrix, and applying boundary conditions, equation (11) will be converted to the following general governing equation:

$$\mathbf{M}^G \ddot{\boldsymbol{\delta}}^G + \mathbf{K}^G \boldsymbol{\delta}^G = 0, \quad (12)$$

where  $\mathbf{K}^G$  and  $\mathbf{M}^G$  are the global stiffness and mass matrices of structures, respectively, and  $\boldsymbol{\delta}^G$  is the global displacement vector of structures.

The solution of the eigenvalue problem is

$$|\mathbf{K}^G - \omega^2 \mathbf{M}^G| = 0, \quad (13)$$

where the  $i$ th eigenvalue  $\omega_i$  is the  $i$ th-order natural frequency.

In this study, FEM is implemented in ANSYS to solve the above problem. Triangular SHELL 181 is used, each node of which has 6 degrees of freedom (three displacements and three rotations).

## 4. Optimization Formulation and Algorithm

**4.1. Statement of Optimization Problem.** In this study, the objective of the optimization is to find optimal geometrical shape and stacking sequence simultaneously to obtain maximum fundamental frequency, which leads to largest stiffness of structures. As presented above, NURBS is employed to describe geometrical shapes with the coordinates of control points as optimization variables. For the sake of simplicity and computational efficiency, only the vertical coordinates in the global coordinate system (as shown in Figure 2), i.e.,  $Z$  coordinates, of control points are determined as variables, while their  $X$  and  $Y$  coordinates are fixed in the optimization process. Meanwhile, the fiber angles of each layer are determined as optimization variables. Here, four possible angles are considered, which are  $0^\circ$ ,  $\pm 45^\circ$ , and  $90^\circ$ . It is noted that the shape variables are continuous, while the variables with respect to stacking sequence are discrete variables. The optimization problem is formulated as follows:

$$\begin{aligned} \text{Max} \quad & f = \text{fundamental frequency,} \\ \text{Design variables} \quad & Z_i (i = 1, 2, \dots, np), \\ & \theta_j (j = 1, 2, \dots, nl), \\ \text{Subject to} \quad & Z_{lb} \leq Z_i \leq Z_{ub}, \\ & \theta_j \in \{0^\circ, \pm 45^\circ, 90^\circ\}, \end{aligned} \quad (14)$$

where  $f$  denotes the optimization objective, which is determined as fundamental frequency in this work.  $Z_i$  is the  $Z$  coordinate of  $i$ th control points with lower and upper bounds  $Z_{lb}$  and  $Z_{ub}$ ,  $np$  is the total number of control points,  $\theta_j$  is the fiber angle of the  $j$ th layer, and  $nl$  is the total number of layers.

**4.2. MIGA Optimization.** GAs are stochastic search techniques based on the mechanism of natural selection and natural genetics [30–32]. One advantage of GAs is that they can find the global optimum and avoid being trapped at a local optimum. Furthermore, different from gradient-based methods, differentiation of objective functions is completely avoided in GAs. In addition, GAs work on the chromosome, which is the encoded version of variables of potential solutions instead of variables themselves. This allows for an efficient optimization involving either continuous or discrete variables [31, 33]. These characteristics are the main reasons for selecting GA in this work. MIGA is developed from the traditional GA and can avoid the “premature” phenomenon, which exists in

general GAs [34, 35]. Therefore, MIGA is applied in this paper to solve the proposed optimization problem (equation (14)). The flow chart of the optimization approach is illustrated in Figure 3, and the details are presented as follows.

Same to other GAs, the algorithm firstly generates a random initial population and encode individuals. As aforementioned, the algorithm needs to deal with continuous and discrete variables simultaneously, which is used to describe geometrical shapes and fiber orientations, respectively. In this algorithm, the continuous variables are written as binary numbers directly, while the discrete variables are transferred into a set of integers, which are then encoded by binary numbers. For example, the four possible values  $0^\circ$ ,  $\pm 45^\circ$ , and  $90^\circ$  in the current study would be represented by four consecutive integers 0, 1, 2, and 3. All binary codes of continuous and discrete variables would be combined as a chromosome for generic operations. It is noted that to decrease the Hamming distance between the adjacent integers, the gray code is used here instead of the traditional binary code.

The fitness values of each individual are calculated by FEM coupled with NURBS. Then, the population of individuals is divided into several subpopulations named “islands,” which is main feature of the MIGA that distinguished it from other GAs. All traditional genetic operations including selection, crossover, and mutation are performed independently on each island. Here, the selection is based on the tournament selection scheme, which is based on the relative tournament size and elite size [36]. The operations of crossover and mutation are determined by crossover and mutation rate, respectively. After the above genetic operations, some individuals are selected from some islands and migrated to different islands periodically. The migration is performed based on the interval of migration. The island of migration is selected randomly, and individuals are exchanged between selected islands according to the migration rate [37]. This process is repeated until a convergence criterion is satisfied. In this study, the convergence criterion is set up in the form of a maximum number of generations without improvement in the best value and average value of a generation.

In the numerical algorithm, MIGA is implemented by commercial software Isight. NURBS and finite element model generation code is written in Fortran, which outputs the ANSYS parametric design language (APDL) file for finite element analysis using ANSYS. Both Fortran code and ANSYS are linked with Isight.

## 5. Numerical Examples and Discussion

The proposed optimization method is applied to the design of a class of laminated square shells, which is a typical design problem in real engineering. The shells are made of a kind of carbon fiber-reinforced polymer (CFRP) material named T300/7901. The stacking sequence through entire shells is uniform. The material parameters are listed in Table 1 referring to [38]. All shells in this section are 16-layer symmetric laminate composite shells, with the thickness of each

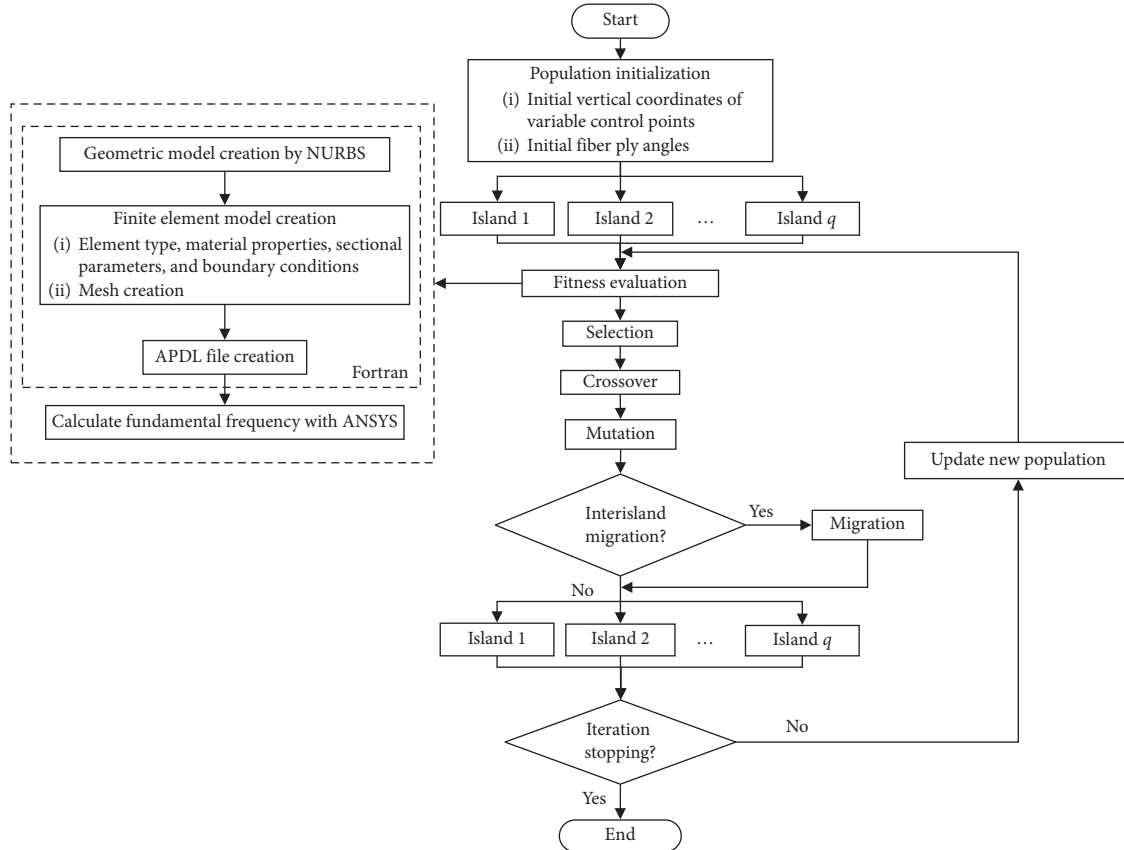


FIGURE 3: Flow chart of MIGA optimization process.

TABLE 1: Material parameters of CFRP material T300/7901.

Longitudinal modulus $E_1$ (GPa)	Transverse modulus $E_2$ (GPa)	Poisson's ratio $\nu_{12}$	Density $\rho$ ( $\text{kgm}^{-3}$ )	Shear modulus $G_{12}$ (GPa)	Shear modulus $G_{13}$ (GPa)	Shear modulus $G_{23}$ (GPa)
138	11	0.28	1690	6	6	3.7

layer assumed to be 1.25 mm, i.e., the thickness of shells is 20 mm.

Three examples are presented. Example 1 presents the simultaneous optimization of square laminated shells considering various boundary conditions. Following that, the so-called two-phase optimization method is applied in Example 2, in which shape optimization and stacking sequence optimization are separately performed. The results are compared with that obtained by simultaneous optimization approach in Example 1. Example 3 repeats the optimization of Example 1 with increased number of control points to investigate the effect of control points on optimal results.

As presented in Section 4, the optimization is carried out by the integration of FEM, NURBS, and MIGA (Figure 3). The MIGA parameters are determined as shown in Table 2.

**5.1. Example 1: Simultaneous Optimization of Square Laminated Shells.** Three square shells with same plane dimension ( $1.6 \times 1.6$  m) and various boundary conditions are

considered here, as depicted in Figure 4. The three shells are simply supported at the four corners (Figure 4(a)), at the two opposite edges (Figure 4(b)) and at the four edges (Figure 4(c)), denoted as Shell 1, Shell 2, and Shell 3, respectively. The proposed simultaneous shape and stacking sequence approach is performed on them to obtain maximum fundamental frequency.

The shapes of shells are designed to be symmetric. NURBS functions are used to represent their geometrical configurations. Considering the symmetry of boundary conditions, the shapes of Shell 1 and Shell 3 are symmetric to  $X$ -axis,  $Y$ -axis, and diagonal lines, while the shape of Shell 2 is only symmetric to  $X$ -axis and  $Y$ -axis. Consequently, the control points of each shell are located as shown in Figure 4, denoted by dots, the number of which is 6, 9, and 6, respectively. In the optimization process, the  $Z$  coordinates of control points on the surface (red dots) are set up as variables, with a feasible domain  $[-0.6 \text{ m}, 0.6 \text{ m}]$ , while control points at the edges (black dots) are fixed meaning the shape and location of edges are not changing in the optimization. Thus, the number of variable control points for Shell 1, Shell

TABLE 2: MIGA parameters.

Subpopulation size	Crossover rate	Migration interval	Number of islands	Mutation rate	Elite size	Number of generations	Migration rate	Relative tournament size
10	1.0	5	10	0.01	1	20–300	0.01–0.5	0.5

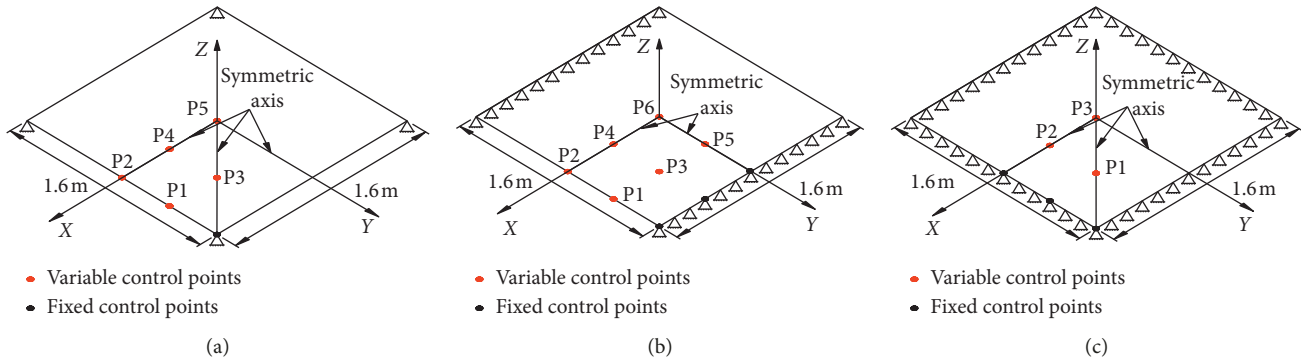


FIGURE 4: Geometry of shells and corresponding location of control points in Example 1. (a) Shell 1. (b) Shell 2. (c) Shell 3.

2, and Shell 3 is 5, 6, and 3, respectively. The basis degrees in the two directions, which were explained in equation (1), are both determined as 2. The weight factors of all control points are set up as 1.0. Note that the basis degrees and weights are not changing in the optimization process.

Simultaneously, fiber angles are set up as variables. As aforementioned, all shells are 16-layer symmetric laminate composite shells. Taking the advantage of the symmetry, the number of variable fiber angles is 8. The fiber angle  $\theta_j$  ( $j = 1, 2, \dots, 8$ ) has four possible values:  $0^\circ$ ,  $\pm 45^\circ$ , and  $90^\circ$ .

The optimization problems are solved by using the proposed optimization algorithm (Figure 3). The MIGA parameters are given in Table 2. The migration rate is determined as 0.01 since the number of variables is relatively small. SHELL 181 in ANSYS is adopted to solve fundamental frequency.

Prior to the optimization, the mesh sensitivity study is carried out. Taking Shell 3 as an example, the Z coordinates of control points P1, P2, and P3 on Shell 3 are assumed to be 0.3 m, 0.1 m, and 0.0 m, respectively. The stacking sequence is determined as  $[-45^\circ/90^\circ/45^\circ_2/90^\circ/-45^\circ/0^\circ/45^\circ]_s$ . The finite element analysis is repeated with various numbers of elements, from 512 to 12800. The fundamental frequency with respect to the different number of elements is illustrated in Figure 5. It can be seen that when the number of element is increased from 512 to 3200, the fundamental frequency is changed remarkably; when the number is larger than 3200, the fundamental frequency is affected slightly by the mesh number. Thus, the number of element is determined as 3200. In the same way, the element numbers of Shells 1 and 2 are also determined as 3200.

MIGA optimization is sequentially performed on Shells 1–3. The best objective value of each generation and the average objective value of each generation are depicted in Figure 6 to show the evolution processes. It can be seen that, in all the cases, the optimization converges within 100 generations. Through the evolution, as shown in Table 3, the

average objective value of generations is increased by 346.32% (Shell 1), 212.62% (Shell 2), and 57.01% (Shell 3), respectively; the best objective value is increased by 94.50% (Shell 1), 43.34% (Shell 2), and 31.50% (Shell 3), respectively. It illustrates that the less constraint at the edges could lead to larger increase in space for the objective value when the location of edges is fixed in the optimization. The individual with the best objective value in the final generation is selected as the optimal result. The optimal lay-up sequences for Shells 1–3 are, respectively,  $[-45^\circ/90^\circ/45^\circ/90^\circ/45^\circ_2/-45^\circ_2]_s$ ,  $[90^\circ/0^\circ/-45^\circ_2/45^\circ/-45^\circ/90^\circ/0^\circ]_s$ , and  $[-45^\circ/90^\circ/45^\circ_2/90^\circ/-45^\circ/0^\circ/45^\circ]_s$ , with various optimal shapes shown in Figure 7.

**5.2. Example 2: Comparison between Simultaneous Optimization and Two-Phase Optimization.** For comparison, the optimization of Shell 1 is reperformed by the so-called two-phase optimization method, the procedure of which is implemented in two uncoupled steps. The process begins with the shape optimization, in which a prescribed lay-up sequence is given, named initial lay-up, and not changing in the optimization process. Then, it is followed by the stacking sequence optimization, in which the shape is fixed as the optimal shape solved by the last step. In this example, both steps are performed by using MIGA. To study the sensitivity of initial lay-ups, the optimization is repeated with three different initial lay-ups, which are  $[45^\circ/-45^\circ_2/45^\circ]_{2s}$ ,  $[0^\circ/90^\circ_2/0^\circ]_{2s}$ , and  $[0^\circ]_{8s}$ . The control points, meshes, NURBS parameters, and MIGA parameters are the same as those in Example 1.

The evolution processes of shape optimization (first phase) with respect to various initial lay-ups are depicted in Figure 8, with optimization results given in Table 4 and Figure 9. Through the shape optimization, the objective value, i.e., fundamental frequency, is increased. However, it is found that there exist considerable differences among the optimal shapes with respect to different initial lay-ups

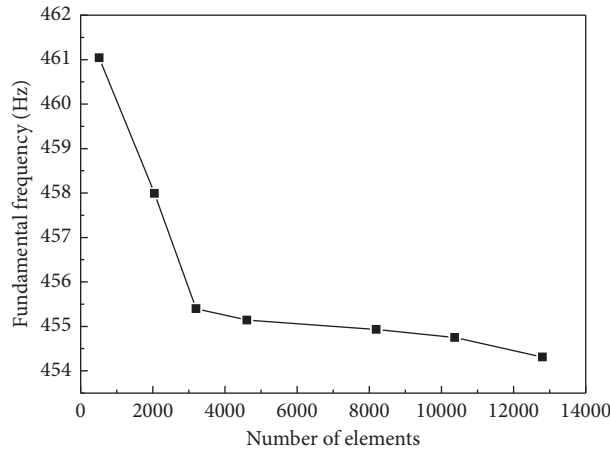


FIGURE 5: Mesh sensitivity study.

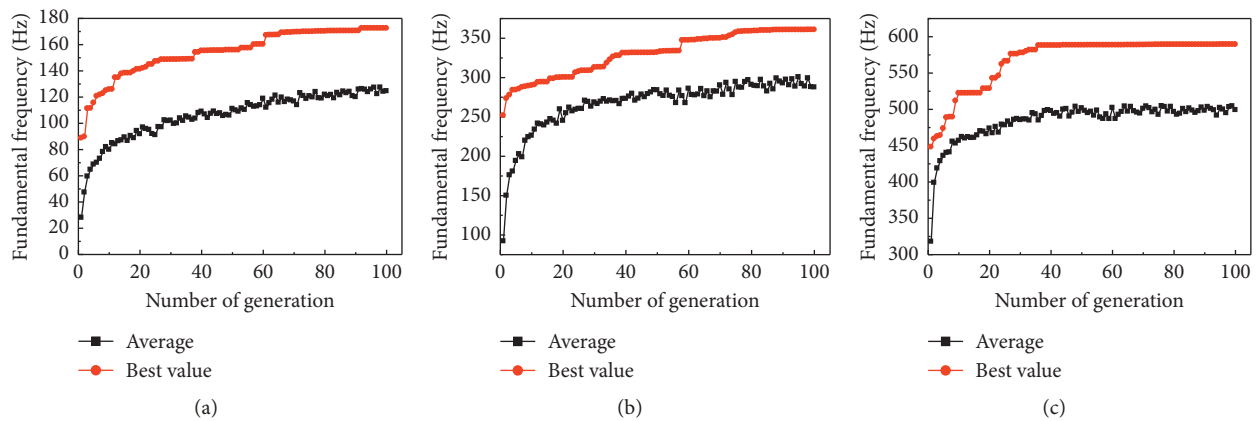


FIGURE 6: Evolution processes of MIGA in Example 1. (a) Shell 1. (b) Shell 2. (c) Shell 3.

TABLE 3: Comparison of fundamental frequency of initial and final generations in Example 1 (Hz).

	Initial generation		Final generation		Relative increase (%)	
	Average	Best	Average	Best	Average	Best
Shell 1	27.89	88.62	124.48	172.37	346.32	94.50
Shell 2	91.97	251.56	287.52	360.59	212.62	43.34
Shell 3	317.80	448.00	498.98	589.12	57.01	31.50

(Figure 9). The optimal shape with respect to initial lay-up  $[0^\circ/90^\circ_2/0^\circ]_{2s}$  (Figure 9(b)) is closer to the optimal shape obtained by simultaneous optimization (Figure 7(a)), while the other two (Figure 9(a) and 9(c)) are significantly different from the simultaneous optimization result. It is illustrated that, the optimal shape is sensitive to the initial lay-up.

The second phase optimization, stacking sequence optimization, is performed based on the optimal shapes (Figure 9).

Figure 10 shows fast convergences of MIGA since only fiber angles are set up as variables with 4 possible values, i.e., the searching space is relative small. The optimal results

are given in Table 5. It can be seen that the fundamental frequency is increased relatively small compared with the shape optimization phase. It agrees with that the geometrical shape plays a more important role than stacking sequence on the mechanical performance of shells. It is also noted that the optimal lay-ups of the three cases are also different, which is mainly caused by the variety of optimal shapes.

Through the two-phase optimization, the optimal fundamental frequency of Shell 1 with different initial lay-ups is increased to be 163.49, 167.79, and 137.86 Hz, respectively. The first two results are slightly smaller than the result of simultaneous optimization in Example 1, which is 172.37 Hz, while the result of the third case is significantly smaller than that of simultaneous optimization by a relative difference of 20.00%. It is clarified that the two-phase optimization tends to seize the local suboptimal results, irrespective of the coupled effect of shape and stacking sequence. The quality of suboptimal results strongly depends on the given initial stacking sequence. In contrast, the simultaneous optimization is searching the global optimal result considering the coupled effect of shape and stacking sequence.

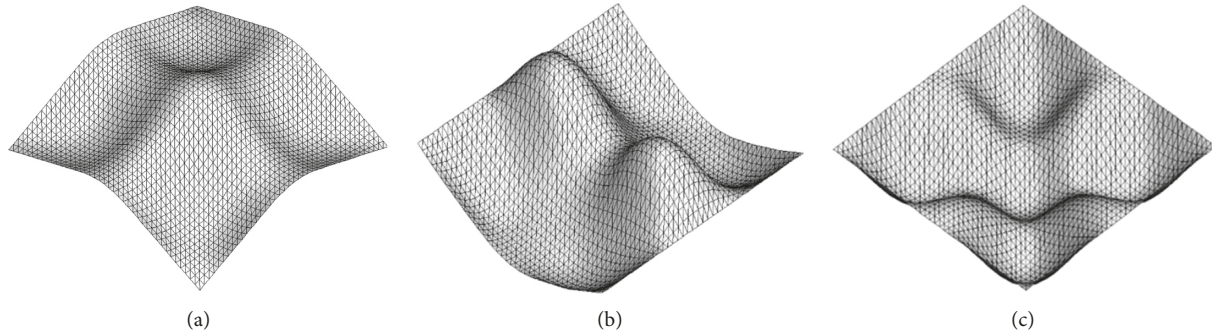


FIGURE 7: Optimal shapes and stacking sequences obtained by simultaneous optimization in Example 1. (a) Shell 1  $[-45^\circ/90^\circ/45^\circ/90^\circ/45^\circ_2/-45^\circ_2]_s$ ; (b) Shell 2  $[90^\circ/0^\circ/-45^\circ_2/45^\circ/-45^\circ/90^\circ/0^\circ]_s$ ; (c) Shell 3  $[-45^\circ/90^\circ/45^\circ_2/90^\circ/-45^\circ/0^\circ/45^\circ]_s$ .

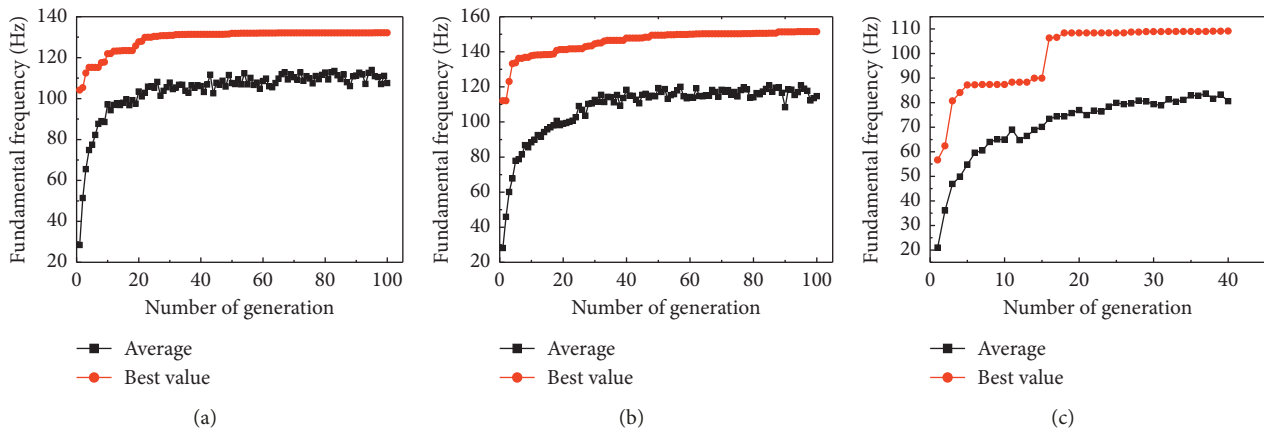


FIGURE 8: MIGA evolution of shape optimization for Shell 1 with different initial lay-ups. (a) Initial lay-up  $[45^\circ/-45^\circ_2/45^\circ]_{2s}$ . (b) Initial lay-up  $[0^\circ/90^\circ_2/0^\circ]_{2s}$ . (c) Initial lay-up  $[0^\circ]_{8s}$ .

TABLE 4: Objective values of initial and final generations in first phase optimization for Shell 1 (Hz).

Initial lay-up ( $^\circ$ )	Initial generation		Final generation		Relative increase (%)	
	Average	Best	Average	Best	Average	Best
$[45/-45_2/45]_{2s}$	28.43	104.11	107.53	132.12	278.23	26.90
$[0/90_2/0]_{2s}$	28.13	112.10	114.68	151.50	307.68	35.15
$[0]_{8s}$	20.95	56.69	80.61	109.17	284.77	92.57

5.3. Example 3: Simultaneous Optimization with Increased Number of Variable Control Points.

The purpose of this example is to explore the potential of simultaneous shape and stacking sequence optimization. For this aim, the numbers of NURBS control points of Shells 1–3 in Example 1 are increased here by two approaches to enlarge shape variety spaces. By Approach 1, as shown in Figure 11, the authors increase the number of control points of Shells 1–3 from 6, 9, 6 to 15, 25, 15, respectively. However, the four edges are still fixed in the optimization process. Thus, the number of variable control points, i.e., shape variables, is 14, 20, and 10, respectively. By Approach 2, as shown in Figure 12, the authors keep the number and locations of control points the same to those

in Example 1 while switch the fixed control points at the edges to variable points, meaning offer variety space for edges. Since Shell 1 has only 4 control points at the edges, all of them need to be fixed. Thus, Approach 2 is only implemented on Shell 2 and Shell 3. By Approach 2, the number of shape optimization variables of Shell 2 and Shell 3 is increased up to 8 and 5, respectively. The optimization variables with respect to stacking sequence are determined the same as in Example 1.

NURBS functions are employed to represent shapes. Mesh size is set up to be the same as in Example 1 since the dimensions remain same. MIGA is used to solve the simultaneous optimization problem. Since the number of optimization variables is increased considerably by Approach 1, the migration rate in Approach 1 cases is increased up to 0.5. In other cases, the migration rate is still set up as 0.01. Other MIGA parameters are the same as in Example 1, as shown in Table 2.

The MIGA evolution processes are given in Figures 13 and 14. It can be seen that the optimizations with respect to Approach 1 converge slower than that Example 1 does, especially in cases of Shell 2 and Shell 3, which needs 300 and 150 generations to converge. That is due to the significant increasing of number of optimization variables. In contrast, the convergence process of shells with respect to Approach 2

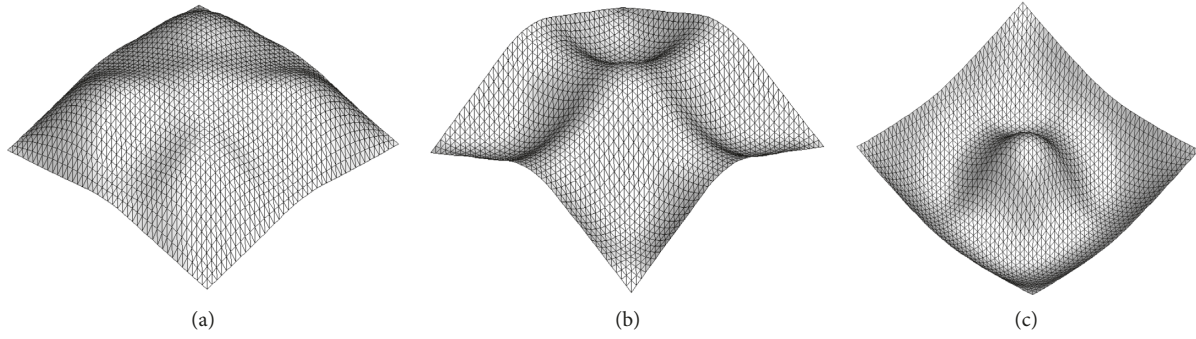


FIGURE 9: Optimal shapes of Shell 1 obtained by the first phase optimization with different initial lay-ups. (a) Initial lay-up  $[45^\circ/-45^\circ_2/45^\circ]_{2s}$ . (b) Initial lay-up  $[0^\circ/90^\circ_2/0^\circ]_{2s}$ . (c) Initial lay-up  $[0^\circ]_{8s}$ .

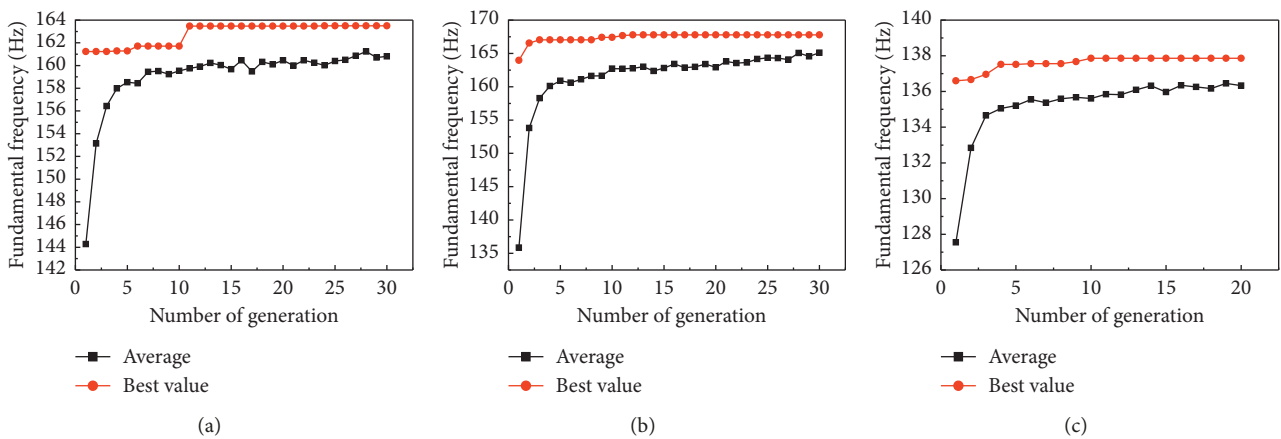


FIGURE 10: MIGA evolution of stacking sequence optimization for Shell 1 with different initial lay-ups. (a) Initial lay-up  $[45^\circ/-45^\circ_2/45^\circ]_{2s}$ . (b) Initial lay-up  $[0^\circ/90^\circ_2/0^\circ]_{2s}$ . (c) Initial lay-up  $[0^\circ]_{8s}$ .

TABLE 5: Optimization results of the second phase optimization for Shell 1 (Hz).

Initial lay-up ( $^\circ$ )	Optimal lay-up ( $^\circ$ )	Initial generation		Final generation		Relative increase (%)	
		Average	Best	Average	Best	Average	Best
$[45/-45_2/45]_{2s}$	$[90/0/45/-45/0/90/45/-45]_s$	144.28	161.23	160.80	163.49	11.45	1.40
$[0/90_2/0]_{2s}$	$[90/0/90/-45/45/90/45/-45]_s$	135.86	163.97	165.11	167.79	21.53	2.33
$[0]_{8s}$	$[0/90/0/45/-45/45/90/0]_s$	127.55	137.60	136.33	137.86	6.88	0.19

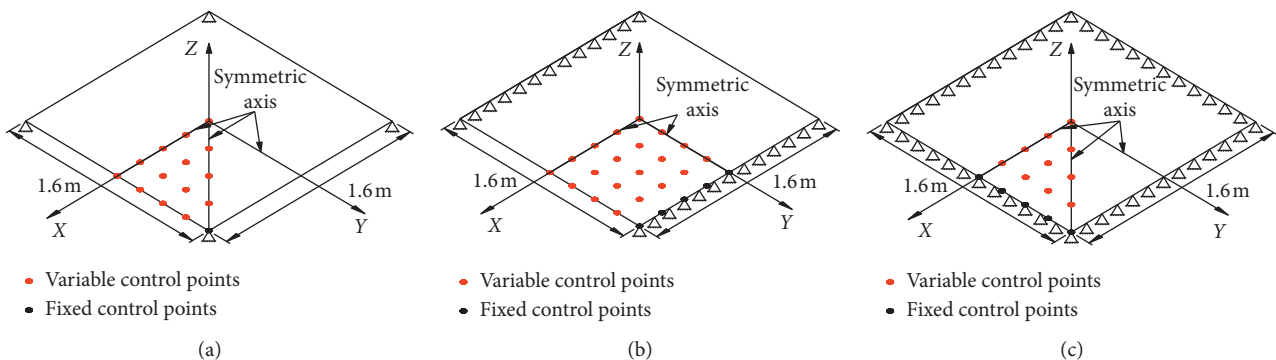


FIGURE 11: Location of control points through Approach 1. (a) Shell 1. (b) Shell 2. (c) Shell 3.

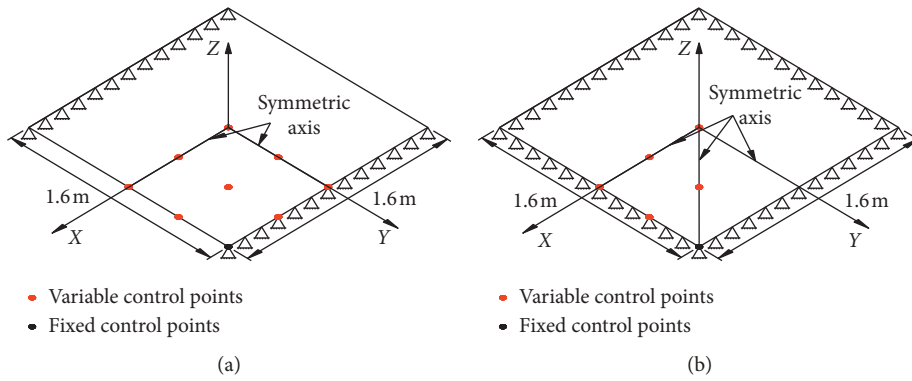


FIGURE 12: Location of control points through Approach 2. (a) Shell 2. (b) Shell 3.

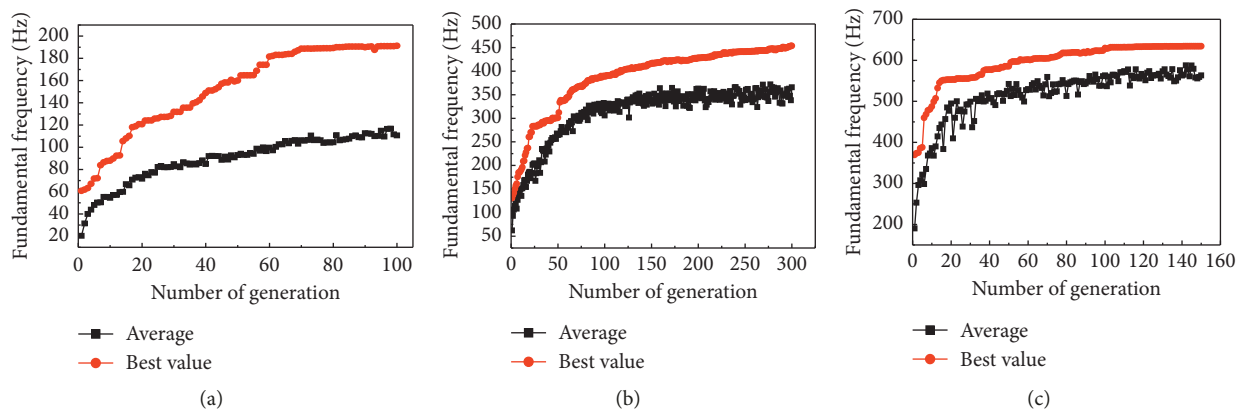


FIGURE 13: MIGA evolution with increased numbers of variable control points (Approach 1). (a) Shell 1. (b) Shell 2. (c) Shell 3.

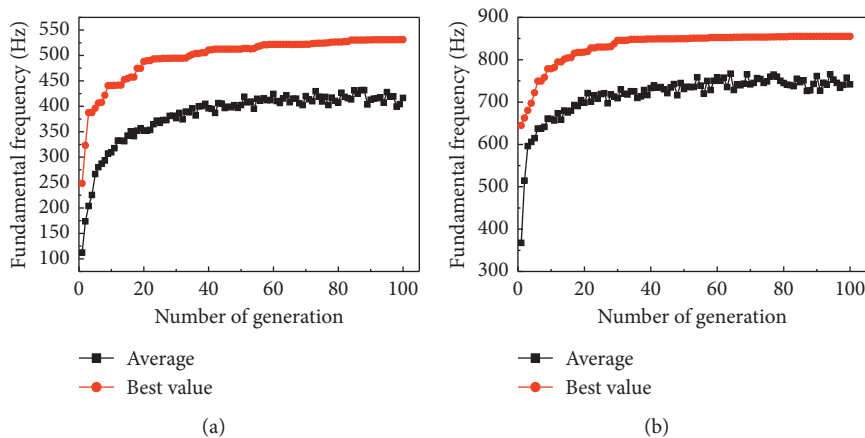


FIGURE 14: MIGA evolution with increased numbers of variable control points (Approach 2). (a) Shell 2. (b) Shell 3.

is similar to that in Example 1 since the number of variables is changed slightly.

The maximum fundamental frequencies, i.e., optimal objective values, of shells with increased numbers of control points are presented and compared with Example 1 in Figure 15. It is found that, both Approaches 1 and 2 increase the optimal objective values. By Approach 1, the maximum

fundamental frequency of Shells 1–3 is increased from 172.37, 360.59, and 589.12 Hz to 191.23, 453.60, and 634.30 Hz, with a relative increase of 10.94%, 25.79%, and 7.60%, respectively. By Approach 2, the maximum fundamental frequency of Shells 2 and 3 is increased up to 531.03 and 855.11 Hz, with a relative increase of 47.27% and 45.15%, respectively. Obviously, fundamental frequency, i.e., the

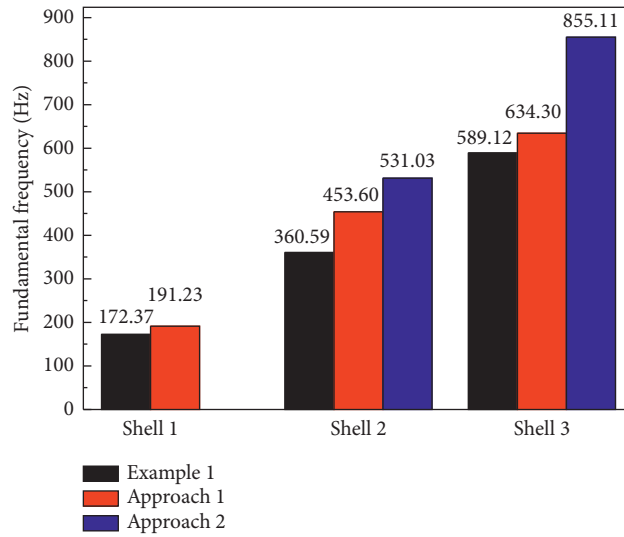


FIGURE 15: Comparison of optimal results by Approaches 1 and 2 and Example 1.

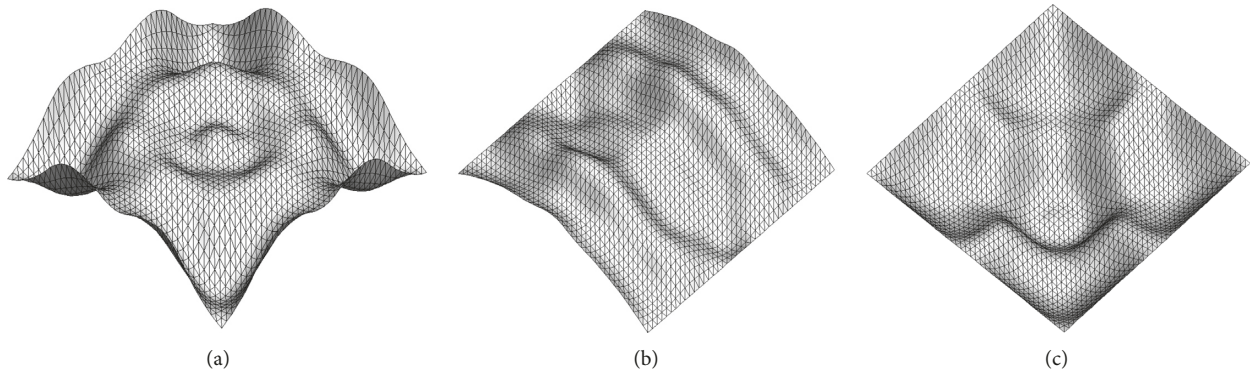


FIGURE 16: Optimal shapes and stacking sequences with increased number of variable control points (Approach 1). (a) Shell 1  $[-45^{\circ}/90^{\circ}/0^{\circ}/90^{\circ}/0^{\circ}/45^{\circ}/-45^{\circ}/45^{\circ}]_s$ . (b) Shell 2  $[0^{\circ}/90^{\circ}/45^{\circ}/0^{\circ}/-45^{\circ}_2/90^{\circ}/-45^{\circ}]_s$ . (c) Shell 3  $[45^{\circ}/0^{\circ}/-45^{\circ}/90^{\circ}/0^{\circ}/90^{\circ}/-45^{\circ}/45^{\circ}]_s$ .

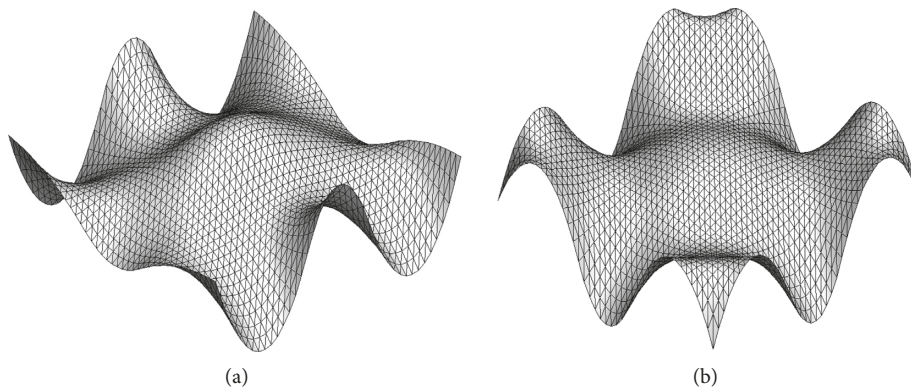


FIGURE 17: Optimal shapes and stacking sequences with increased number of variable control points (Approach 2). (a) Shell 2  $[0^{\circ}/90^{\circ}/-45^{\circ}_2/45^{\circ}/-45^{\circ}/0^{\circ}_2]_s$ . (b) Shell 3  $[-45^{\circ}/0^{\circ}/90^{\circ}/45^{\circ}_2/0^{\circ}/90^{\circ}/-45^{\circ}]_s$ .

objective value, is increased more remarkably by Approach 2 than by Approach 1.

The optimal shapes together with optimal stacking sequences with respect to Approach 1 are presented in

Figure 16. Compared to Example 1 (Figure 7), the optimal shapes of Shells 1 and 2 are changed significantly by Approach 1. The increase of the variable control points leads to more waves on the surface, as well as higher objective value

as aforementioned. On the contrary, the optimal shape of Shell 3 seems to be similar to that in Example 1 (Figure 7(c)). The reason is considered to be that the four edges of Shell 3 are fixed, which leads to a relative small optimization space, and thus the increase of number control points does not affect the optimal shape significantly. However, the curvature of the surface is increased. Therefore, the objective value, i.e., fundamental frequency, is increased to some extent. As a result of shape variety, the optimal stacking sequences are also different from that in Example 1.

The optimal shapes together with optimal stacking sequences of shells implemented by Approach 2 are presented in Figure 17. It can be observed that compared to Example 1, the change of optimal shapes mainly occurs on the edges, which sequentially leads to the geometrical change of the entire surface. The surfaces remain smooth all over the shells since the number of variable control points on the surface is not increased. In addition, the optimal stacking sequence of shells is also different from Example 1 and the cases of Approach 1.

To sum up, increasing the number of control points introduces more degrees of freedom in the optimization and would result in improved optimal results. Compared to adding variable control points on the surface of shells, it is more efficient to add variable control points at the edges.

## 6. Conclusions

A numerical algorithm for simultaneous shape and stacking sequence optimization of laminated composite free-form shells is developed. The fundamental frequency is determined as the objective function, and vertical coordinates of NURBS control points together with fiber ply angles are simultaneously set up as design variables. MIGA coupled with FEM and NURBS is employed to obtain optimal results. Three numerical examples are presented, and the main conclusions are obtained as follows: (i) Through the simultaneous optimization examples, the efficiency and convergence of the proposed method is demonstrated. The boundary conditions have a great effect on the optimal results. Generally, the less constraint at the edges leads to larger increase on the objective value. (ii) By comparison, it is clarified that the two-phase optimization is actually seizing local suboptimal results, irrespective of the coupled effect of shape and stacking sequence. The quality of suboptimal results strongly depend on the given initial stacking sequence. In contrast, the simultaneous optimization can obtain the global optimal result that considers the coupled effect of shape and stacking sequence. (iii) Increasing the number of control points introduces more degrees of variety freedom in the optimization and would result in improved optimal results. Compared to adding variable control points on the surface of shells, it is more efficient to add variable control points at edges.

## Data Availability

The data used to support the findings of this study are available from the corresponding author upon request.

## Conflicts of Interest

The authors declare that there are no conflicts of interest regarding the publication of this paper.

## Acknowledgments

The authors would like to acknowledge the National Natural Science Foundation of China (grant no. 51578211) and the Fundamental Research Funds for the Central Universities (grant no. 2018B13814) for supporting this research.

## References

- [1] X. Liu, C. A. Featherston, and D. Kennedy, "Two-level layout optimization of composite laminate using lamination parameters," *Composite Structures*, vol. 211, pp. 337–350, 2019.
- [2] Y. Dai, M. Feng, and M. Zhao, "Topology optimization of laminated composite structures with design-dependent loads," *Composite Structures*, vol. 167, pp. 251–261, 2017.
- [3] J. Wu and R. Burgueno, "An integrated approach to shape and laminate stacking sequence optimization of free-form FRP shells," *Computer Methods in Applied Mechanics and Engineering*, vol. 195, no. 33–36, pp. 4106–4123, 2006.
- [4] R.-Q. Feng and J.-M. Ge, "Shape optimization method of free-form cable-braced grid shells based on the translational surfaces technique," *International Journal of Steel Structures*, vol. 13, no. 3, pp. 435–444, 2013.
- [5] M. Bagneris, R. Motro, B. Maurin, and N. Pauli, "Structural morphology issues in conceptual design of double curved systems," *International Journal of Space Structures*, vol. 23, no. 2, pp. 79–87, 2008.
- [6] W. A. Wall, M. A. Frenzel, and C. Cyron, "Isogeometric structural shape optimization," *Computer Methods in Applied Mechanics and Engineering*, vol. 197, no. 33–40, pp. 2976–2988, 2008.
- [7] K.-U. Bletzinger, R. Wüchner, F. Daoud, and N. Camprubi, "Computational methods for form finding and optimization of shells and membranes," *Computer Methods in Applied Mechanics and Engineering*, vol. 194, no. 30–33, pp. 3438–3452, 2005.
- [8] J. Kiendl, R. Schmidt, R. Wüchner, and K.-U. Bletzinger, "Isogeometric shape optimization of shells using semi-analytical sensitivity analysis and sensitivity weighting," *Computer Methods in Applied Mechanics and Engineering*, vol. 274, no. 6, pp. 148–167, 2014.
- [9] H. Ohmori and H. Hamada, "Computational morphogenesis of shells with free curved surface considering both designer's preference and structural rationality," in *Proceeding of IASS-APCS*, vol. 274, pp. 512–513, Beijing, China, October 2006.
- [10] M. Shimoda and Y. Liu, "Free-form optimization of thin-walled structure for frequency response problem," *Shock and Vibration*, vol. 2015, Article ID 471646, 11 pages, 2015.
- [11] M. Shimoda and Y. Liu, "Node-based free-form optimization method for vibration problems of shell structures," *Computers & Structures*, vol. 177, pp. 91–102, 2016.
- [12] P. Winslow, S. Pellegrino, and S. B. Sharma, "Multi-objective optimization of free-form grid structures," *Structural and Multidisciplinary Optimization*, vol. 40, no. 1–6, pp. 257–269, 2010.
- [13] B. Kriegesmann, R. Rolfes, E. L. Jansen, I. Elishakoff, C. Hühne, and A. Kling, "Design optimization of composite cylindrical shells under uncertainty," *Computers Materials and Continua*, vol. 32, no. 3, pp. 177–200, 2012.

- [14] M. Abouhamze and M. Shakeri, "Multi-objective stacking sequence optimization of laminated cylindrical panels using a genetic algorithm and neural networks," *Composite Structures*, vol. 81, no. 2, pp. 253–263, 2007.
- [15] E. Ameri, M. M. Aghdam, and M. Shakeri, "Global optimization of laminated cylindrical panels based on fundamental natural frequency," *Composite Structures*, vol. 94, no. 9, pp. 2697–2705, 2012.
- [16] S. Zhi, S. Shanshan, and C. Haoran, "Buckling and optimal analysis for advanced composite conical shells stiffened by non-uniform distribution grids," in *Proceeding of International Conference on Composite Structures*, Porto, Portugal, June 2011.
- [17] R. Mingfa, B. Fanzi, and T. Li, "Structural optimization approach for specially shaped composite tank in spacecrafts," *Journal of Mechanical Science and Technology*, vol. 29, no. 4, pp. 1429–1435, 2015.
- [18] U. Topal, "Frequency optimization of laminated composite spherical shells," *Science and Engineering of Composite Materials*, vol. 19, no. 4, pp. 381–386, 2012.
- [19] R. Nascimbene, "Analysis and optimal design of fiber-reinforced composite structures: sail against the wind," *Wind and Structures*, vol. 16, no. 6, pp. 541–560, 2013.
- [20] S. Nikbakt, S. Kamarian, and M. Shakeri, "A review on optimization of composite structures Part I: laminated composites," *Composite Structures*, vol. 195, pp. 158–185, 2018.
- [21] H. Ghiasi, D. Pasini, and L. Lessard, "Optimum stacking sequence design of composite materials Part I: constant stiffness design," *Composite Structures*, vol. 90, no. 1, pp. 1–11, 2009.
- [22] S. Honda, T. Kato, Y. Narita, and D. Narita, "Multidisciplinary design optimization of surface shapes and lay-up configurations for laminated composite shells," *Journal of System Design and Dynamics*, vol. 5, no. 8, pp. 1662–1673, 2011.
- [23] S. Shojaee, E. Izadpanah, N. Valizadeh, and J. Kiendl, "Free vibration analysis of thin plates by using a NURBS-based isogeometric approach," *Finite Elements in Analysis and Design*, vol. 61, pp. 23–34, 2012.
- [24] X. Qian, "Full analytical sensitivities in NURBS based isogeometric shape optimization," *Computer Methods in Applied Mechanics and Engineering*, vol. 199, no. 29–32, pp. 2059–2071, 2010.
- [25] L. Piegl and W. Tiller, *The NURBS Book*, Springer Science and Business Media, Berlin, Germany, 2012.
- [26] X. Li, *Study on Morphology of Freeform Surface Structures*, Ph.D. thesis, Harbin Institute of Technology, Harbin, China, 2011.
- [27] G. Huang, H. Wang, and G. Li, "An efficient reanalysis assisted optimization for variable-stiffness composite design by using path functions," *Composite Structures*, vol. 153, pp. 409–420, 2016.
- [28] H. Nguyen-Van, N. Mai-Duy, and T. Tran-Cong, "Free vibration analysis of laminated plate/shell structures based on FSDT with a stabilized nodal-integrated quadrilateral element," *Journal of Sound and Vibration*, vol. 313, no. 1–2, pp. 205–223, 2008.
- [29] M. K. Apalak, M. Yildirim, and R. Ekici, "Layer optimisation for maximum fundamental frequency of laminated composite plates for different edge conditions," *Composites Science and Technology*, vol. 68, no. 2, pp. 537–550, 2008.
- [30] X. Yu and M. Gen, *Introduction to Evolutionary Algorithms*, Springer, London, UK, 2010.
- [31] M. Mitchell, *An Introduction to Genetic Algorithms*, MIT Press, Cambridge, MA, USA, 1999.
- [32] S. Karakatić and V. Podgorelec, "A survey of genetic algorithms for solving multi depot vehicle routing problem," *Applied Soft Computing*, vol. 27, pp. 519–532, 2015.
- [33] B. San and H. Waisman, "Optimization of carbon black polymer composite microstructure for rupture resistance," *Journal of Applied Mechanics*, vol. 84, no. 2, Article ID 021005, 2016.
- [34] X. Hu, X. Chen, Y. Zhao, and W. Yao, "Optimization design of satellite separation systems based on Multi-Island Genetic Algorithm," *Advances in Space Research*, vol. 53, no. 5, pp. 870–876, 2014.
- [35] W. Wang, S. Yuan, J. Pei, and J. Zhang, "Optimization of the diffuser in a centrifugal pump by combining response surface method with multi-island genetic algorithm," *Proceedings of the Institution of Mechanical Engineers, Part E: Journal of Process Mechanical Engineering*, vol. 231, no. 2, pp. 191–201, 2017.
- [36] N. Jansson, W. D. Wakeman, and J.-A. E. Månson, "Optimization of hybrid thermoplastic composite structures using surrogate models and genetic algorithms," *Composite Structures*, vol. 80, no. 1, pp. 21–31, 2007.
- [37] H. Chen, R. Ooka, and S. Kato, "Study on optimum design method for pleasant outdoor thermal environment using genetic algorithms (GA) and coupled simulation of convection, radiation and conduction," *Building and Environment*, vol. 43, no. 1, pp. 18–30, 2008.
- [38] H. Wang, Y. Duan, D. Abulizi, and X. Zhang, "Design optimization of CFRP stacking sequence using a multi-island genetic algorithms under low-velocity impact loads," *Journal of Wuhan University of Technology-Mater. Sci. Ed.*, vol. 32, no. 3, pp. 720–725, 2017.



**Hindawi**

Submit your manuscripts at  
[www.hindawi.com](http://www.hindawi.com)

